

## Synthesis, structural and electrical characterizations of SnO<sub>2</sub> nanoparticles

N. Manjula<sup>1</sup>, G.Selvan<sup>2</sup>, R. Perumalsamy<sup>3</sup>, R. Thirumamagal<sup>4</sup>, A. Ayeshamariam<sup>5\*</sup> and M. Jayachandran<sup>6</sup>

<sup>1</sup>*Research Scholar, Bharathiyyar University, Coimbatore, India*

<sup>2</sup>*Department of Physics, Thanthai Hans Roever College, Perambalur, India*

<sup>3</sup>*Department of Physics, Theagaraya College Higher Secondary School, Chennai-21, India*

<sup>4</sup>*Department of Physics, Ananadha College, Devakkottai, India*

<sup>5</sup>*Department of Physics, Khadir Mohideen College, Adirampattinam, India*

<sup>6</sup>*Electro Chemical Material Science Division, Central Electro Chemical Research Institute (CSIR), Karaikudi, 630006, India.*

Received 27 July 2015; Accepted 9 Sep. 2015

### Abstract

Sol-gel synthesized SnO<sub>2</sub> nanoparticles with an average size of 20.0 nm obtained at 100° C were gradually annealed to 800° C in air for 60 minutes. Crystal density, lattice volume and microstrain are found to be nearly constant with annealing temperature, which confirm the formation of monophase SnO<sub>2</sub>. The prepared powders were characterized for their structural, morphological, and electrical properties. Spherical particles in the nanoscale level, with the size increasing with temperature are observed from XRD, SEM and TEM results.

**Keywords:** Structural; Morphological; Electrical.

**PACS:** 73.30.+y; 73.40.Ns; 73.40.-c.

### 1. Introduction

Tin oxide received major attention in the sensor mechanisms compared to other metal oxides. Tin oxide has a rutile type crystal structure. Its lattice parameters are:  $a=4.75\text{\AA}$  and  $c=3.19\text{ \AA}$ . The unit cell contains six atoms: two Tin and four oxygen. The specific density is  $6.95\times 10^3\text{ kg/m}^3$ , and its hardness on the Mohs scale is about 7.8, which is even slightly more than the value of glass [1].

Tin dioxide (SnO<sub>2</sub>) is an important oxide semiconductor material, which has been widely used in many applications such as catalysts agent [2,3], hazardous gas sensors [4,5], heat reflecting mirrors [6,7], varistors [8,9], transparent conducting electrodes for solar cells [10,11], and optoelectronic devices [12]. Tin dioxide-based gas sensor devices are very important in developing n-type semiconductor sensors, which can be utilized to detect various inflammable and harmful gases such as hydrogen (H<sub>2</sub>), carbon monoxide (CO), ethanol and methanol. Sensors consisting of fine particles of metal oxides usually exhibit high sensitivity compared to their counterparts made of larger particles. The most important factor affecting the sensitivity of gas sensors is the actual crystallite size of the sensing materials. Hence, semiconductor based sensors should have fine crystallites to achieve high sensitivities [5].

Tin dioxide powders that are used for gas sensors have been synthesized via various routes such as direct strike precipitation [13, 14], two-step solid state synthesis [15], microemulsion [16], sol-gel [17], spray pyrolysis [18], gel combustion technique [19], hydrothermal synthesis [20], etc. Among the above methods, conventionally accepted method is the synthesis of tin dioxide particles from precursor hydroxides precipitated by the direct addition of NH<sub>4</sub>OH to SnCl<sub>4</sub> aqueous solutions. Although, this technique yields a large amount of powder instantaneously and at a reasonable cost, it is not easy to obtain powders with high surface area because of the irregular particle morphology, large particle size distribution and the high degree of agglomeration [13, 14]. Those problems arise due to the non-uniform super saturation in solution.

Franklin Cabrera et al., reported that the addition of 3% Sn produces an important reduction of the amount of oxidized chromium and that the amount of deposited coke improves the catalytic stability but diminish the activity. In all cases, the addition of tin improves the initial selectivity of the catalysts [21].

Jean-Marie Herrmann et al. reported in their paper the characterization of Mo–Sn–O systems by Raman spectroscopy and electrical conductivity measurements. The authors found that four-coordinated species are dispersed at the external surface while six-coordinated species are occluded through coalescence of molybdate layers [22]. Vitor Baranauskas et al., reported that the conductivity of tin oxide films deposited by spray pyrolysis method increases with the increase of the deposition temperature due to the increase in the granular coalescence and thermal decomposition of tin hydroxides [23]. Min-Sik Park et al., reported the electrochemical performances of 1D SnO<sub>2</sub> nanomaterials, (nanotubes, nanowires, and nanopowders) afterward compared to define the most favorable morphology when SnO<sub>2</sub> nanomaterials are adopted as an electrode material for lithium-ion batteries. Changes in the morphology of SnO<sub>2</sub> are closely related with its electrochemical performance.

Some SnO<sub>2</sub> nanomaterials features do not only induce an increase in the energy density but also enhanced Li<sup>+</sup> transfer. The correlation between the morphological characteristics and the electrochemical properties of SnO<sub>2</sub> nanomaterials was discussed. The interesting electrochemical results obtained on SnO<sub>2</sub> nanomaterials indicate the possibility of designing and fabricating attractive new nanostructured materials for lithium-ion batteries [24].

When the size of the particle is tuned to nanosize, it has fewer adjacent coordinated atoms and can be treated as defects as compared with the bulk atoms. These defects induce additional electronic states in the band gap, which can mixed with the intrinsic states to a substantial extent and which may influence the spacing of the energy levels and the optical properties of nanopowders. But its high surface-to-volume ratio in the surface atoms plays a large role in the properties of nanomaterials,

In this article, we report the synthesis of tin oxide nanoparticles by a novel sol-gel combustion technique from tin nitrate. The starting materials are very cheap and the synthesis procedure is simple, and the obtained SnO<sub>2</sub> particles are in the nanometer scale and mono-dispersed with very high surface area. This should be a better choice instead of the sol-gel method from tin alkoxides. The particles have been characterized by means of XRD, TG-DSC, XPS, SEM and EDAX, TEM, electrical properties and sensing performance.

## 2. Method of analysis

Phase identification and crystallite size determination were carried out using PANalytical X’Pert X-ray diffractometer (CuK $\alpha$  target,  $\lambda = 1.5418 \text{ \AA}$ ). XRD data were collected in the  $2\theta$  range of  $20\text{--}80^\circ$  using step scan mode with step width of  $0.02^\circ$  and step time 2.40 s. Appreciable intensity could be obtained with this step width, which was found to be suitable for getting the satisfactory profile shape. Chemical state analysis was conducted using X-ray photoelectron spectroscopy (XPS) using a Multilab-2000 spectrometer using a monochromatic Mg-K $\alpha$  X-ray source (1256 eV) with analyzer pass energy of 10 eV. Surface morphology of the samples was investigated by scanning electron microscopy, (SEM) Hitachi S-3400N and the chemical composition was examined using EDAX attachment Nortan system six attached to the SEM unit. Nanoparticles and structure analysis was carried out using transmission electron microscopic (TEM) instrument. TEM imaging and selected area electron diffraction (SAED) patterns were recorded using a 200 KV Tecnai-20 G2 TEM instrument. The electrical resistivity, mobility and carrier concentration were determined using Hall Effect measurements HMS-3000 VER-3.51.3

## 3. Experimental procedure

Tin oxide nanoparticles were prepared by the sol-gel route as reported in our previous research [25]. Generally, **2.94** g tin nitrate was added to 50 mL ultra-pure water in a round bottom flask and was stirred for 20 min. A certain amount of urea was added into the mixture under a controlled feed rate ( $0.01\text{--}0.1 \text{ mL min}^{-1}$ ) and constant stirring. After 2 h of stirring, the sol was aged at room temperature for 24 h. The solutions were heated under constant stirring at a temperature of about  $90\text{--}100^\circ\text{C}$  in a Pyrex vessel and concentrated slowly without producing any precipitation until it turned into a white and viscous gel. The portions of the gels were heated at temperatures of about  $350^\circ\text{C}$ , which suffered a strong self-propagating combustion reaction with the evolution of a large volume of gases. The entire combustion process was over after a few seconds. The resulting white ashes were then calcined at temperatures in the range 100 to  $800^\circ\text{C}$  for 1 h in order to eliminate the carbonaceous residues. The selection of the tin to fuel ratio and the ignition and calcination temperature were discussed [26].

According to Cooper et al [27], for a stoichiometric combustion reaction between a fuel and an oxidizer, the ratio of the net oxidizing valency of the metal nitrate to the net reducing valency of the fuel should be unity. The total oxidizing valency of  $\text{Sn}(\text{NO}_3)_2 \cdot 2\text{H}_2\text{O}$  works out to be -8. Urea ( $\text{N}_2\text{H}_4\text{CO}$ ) was taken as a fuel, which contains one carboxylic and four hydroxyl group for coordinating the metal ions, which facilitate the formation of a viscous gel. The total reducing valency of urea works out to be +6. Hence in order to have the stoichiometric combustion reaction, one mole of indium nitrate needs  $8/6$  (or 1.333) mol of urea. This ratio of oxidant: fuel (1:1.33) gives a satisfactory viscous gel to initiate combustion. Since oxidant-fuel composition was optimum, sluggish decomposition was not possible and therefore the reaction not leftover carbonaceous material in the as-prepared powder. These observations are in good agreement with those reported in the literature [28]. The further fuel-rich ratios were not suitable due to a sluggish and incomplete combustion.

## 4. Results and discussion

### 4.1 Structural Characterization of SnO<sub>2</sub>

The crystallinity of the sample is clearly evident by the sharper diffraction peaks at respective diffraction angles which can be readily indexed for its tetragonal structure of the as-prepared SnO<sub>2</sub> powder, as shown in Figure 1.

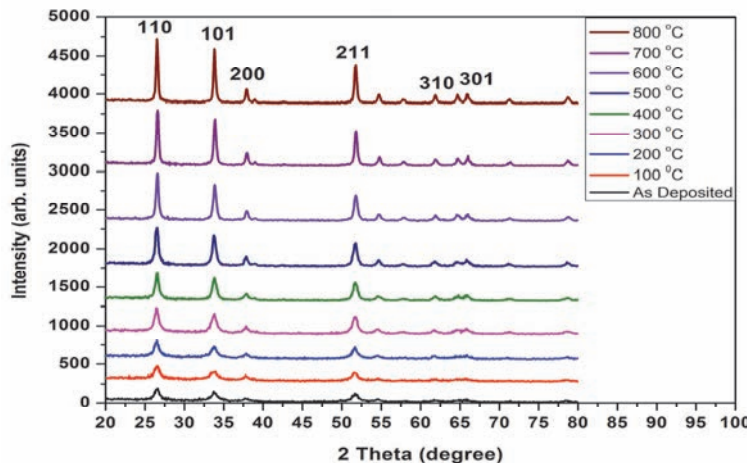


Fig. 1: XRD patterns of SnO<sub>2</sub> nanopowders

The obtained phase is comparable with the standard JCPDS data (Card No. 88-0287). The sample exhibited only the tetragonal phase and the major peaks appeared at  $2\theta = 26.9^\circ$ ,  $34.3^\circ$ ,  $38.9^\circ$ ,  $52.1^\circ$ ,  $62.1^\circ$  and  $65.8^\circ$ . It is further observed that there is no indication of the presence of both low temperature monoclinic or high temperature cubic phases. Evidence of the cubic symmetry might be again confirmed from the non-symmetric line shape around  $2\theta = 20^\circ$  and  $80^\circ$  regions of the XRD pattern. In the  $2\theta = 34.3^\circ$  region, the non-symmetrical line shape originated from broadening of peak 101 and the crystallite size of 14 nm was determined. Similarly, non-symmetrical peaks can be detected at  $2\theta=62.1^\circ$  and  $65.8^\circ$  and indexed as (310) and (301) respectively and the decrease of broadening indicated the growth of the crystallite size from minimum to maximum value, but average crystallite size is around 15 nm for the as-prepared powder.

All of the observed peaks in the XRD pattern in Figure 1 are indexed assuming SnO<sub>2</sub> phase, giving all peaks positions, Miller indices, interplanar distances (observed and standard) their deviations and the micro strain on the grains. The micro strain is developed on the grains and within the grains that can be visualized from the line shifting in the XRD spectra. For the present study, the calculated micro strain in most planes is positive, indicating the presence of tensile stress on the surface of the particles.

The micro strain is proportional to the lattice distortion.

$$\frac{1}{d^2} = \frac{h^2 + k^2}{a^2} + \frac{l^2}{c^2} \quad (2)$$

The observed negative values of micro strain for the planes may be due to induced error in the measurement of the  $2\theta$  value, since the respective peaks are non -symmetrical. The high-angle region of XRD pattern of the as-synthesized powder was used to determine

the lattice parameters ‘a’ and ‘c’ of the tetragonal phase, using the equation (2) [28]. By using this equation, we calculated the values of lattice parameter and are tabulated in table. 1, which well matches with JCPDS file no (Card No. 88-0287)  $a = 4.737\text{\AA}$  and  $c = 3.186\text{\AA}$ .

Table 1: Interplanar  $d_{hkl}$  spacing and microstrain of  $\text{SnO}_2$  nanopowders

Peak position( $2\theta$ )	(hkl)	Interplanar distance ( $d_{hkl}$ ) ( $\text{\AA}$ )		$\frac{d_0 - d_s}{d_s} (\text{\AA})$	MicroStrain $\epsilon = \frac{\Delta d_{hkl}}{d_s}$
		Obs ( $d_0$ )	Std ( $d_s$ )		
26.9877	110	3.349	3.301	0.048	0.014
34.3913	101	2.643	2.627	0.015	0.006
38.3913	200	2.368	2.342	0.025	0.011
52.1348	211	1.764	1.752	0.011	0.006
62.1419	310	1.498	1.492	0.005	0.003
65.8945	301	1.414	1.416	-0.001	-0.001

The specific surface area of as-prepared powdered particle is  $56.318\text{ m}^2/\text{g}$  and annealed at  $800^\circ\text{C}$  is equal to  $33.881\text{ m}^2/\text{g}$ , by increasing temperature reduces the specific surface area shown in Table 2.

Table 2: Crystallite and particle size of nanocrystalline  $\text{SnO}_2$  powders

$\text{SnO}_2$	$D = \frac{0.94\lambda}{\beta \cos \theta}$ (nm)	$a (\text{\AA})$	$c (\text{\AA})$	$S = \frac{6}{\rho D} \text{ m}^2/\text{g}$
Asprepared	15.573	4.758	3.202	56.318
100°C	16.588	4.759	3.182	56.260
200°C	18.154	4.750	3.176	56.4305
300°C	18.979	4.746	3.176	56.295
400°C	19.290	4.745	3.176	61.755
500°C	20.331	4.758	3.169	50.256
600°C	21.313	4.759	3.170	44.815
700°C	21.873	4.752	3.171	39.3199
800°C	22.224	4.750	3.170	33.881

The above values are again verified using cell refinement software for the same tetragonal structure by considering all the indexed peaks. The obtained values for the lattice parameters  $a = 4.737\text{\AA}$  and  $c = 3.186\text{\AA}$  are consistent with the standard JCPDS card No. 88-0287. Similarly, the refined cell constant exactly matches with the standard value and is also in agreement with the reported values. The unit cell volume of a tetragonal lattice is given by the equation (3)

$$V = a^2 * c = 71.4996 \text{ \AA}^3 \quad (3)$$

The calculated and refined values of unit cell volume of the crystal system, also matches well with the standard values shown in Table 3, it can be observed that the cell mass stabilized after  $300^\circ\text{C}$  [29]. The value of the density also stabilized above  $400^\circ\text{C}$ , though the crystallite size is found to increase with increasing annealing temperature.

## 4.2 DTA/TGA Analysis of SnO<sub>2</sub>

Thermogravimetric analysis (TG) measurements were carried out by taking 3.4580 mg of as-prepared SnO<sub>2</sub> in a quartz pan to minimize the effects during decomposition of the sample. The heating program was between 30 and 1100°C and the heating rate was 20°C/min in air, and the purge gas employed was nitrogen at a flow of 45 ml/min. It is observed (Figure 2) that only 13.4% weight loss is noticed in the entire decomposition programme and the weight loss is due to the removal of chemisorbed water molecules during exposure of the sample to the air atmosphere. In support of TGA, simultaneous DTA was recorded in the same temperature range to confirm the decomposition steps (Figure 2).

Table 3: Refined Parameters of the as-prepared SnO<sub>2</sub> nanopowders

	<b>RT</b>	<b>100°C</b>	<b>200°C</b>	<b>300°C</b>	<b>400°C</b>	<b>500°C</b>	<b>600°C</b>	<b>700°C</b>	<b>800°C</b>
a (Å)	4.7505	4.7446	4.746	4.744	4.7446	4.7409	4.7397	4.7408	4.7398
c (Å)	3.1917	3.1865	3.196	3.189	3.1896	3.1886	3.1865	3.1891	3.1876
Crystallite size (nm)	10.3	9.4	10.8	13.3	19.0	30.8	32.0	41.0	49.9
Cell mass (g)	258.943	264.88	280.21	280.52	280.52	280.52	280.52	280.52	280.52
Cell volume (Å <sup>3</sup> )	72.0243	71.732	71.988	71.788	71.802	71.67	71.58	71.677	71.611
Crystal density (g/cm <sup>3</sup> )	5.970	6.132	6.464	6.489	6.488	6.500	6.507	6.499	6.505
R-Bragg	2.686	2.690	3.134	5.042	8.267	6.411	5.619	6.483	6.857
R <sub>wp</sub>	16.30	16.33	16.56	17.13	18.06	28.69	16.68	16.92	17.02
Goodness of fit (GOF)	1.01	1.04	1.05	1.13	1.12	1.87	1.03	1.08	1.08

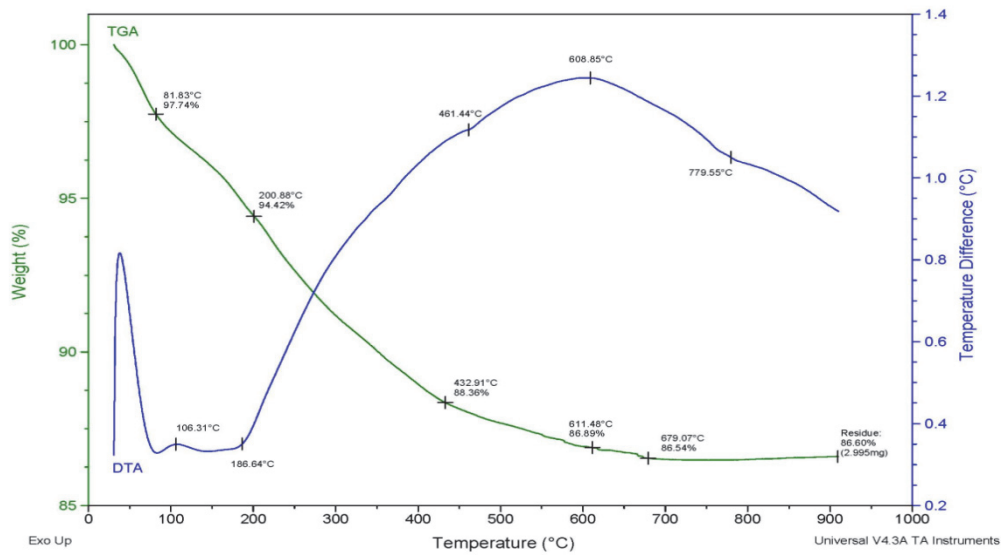


Fig. 2: DTA/TG analysis of as-prepared SnO<sub>2</sub> nanopowder

Chemisorption of adsorbed species or a chemical decomposition is an endothermic process. It occurs by absorbing heat to raise the enthalpy of the system to a critical limit of its thermodynamic stability before it dissociates. This is reflected in the DTA curve and however, there are no noticeable exothermic and endothermic peaks which are visible in the recorded temperature range. It confirms the purity of the as-prepared  $\text{SnO}_2$  powder which is free from all other added organic and inorganic precursors during the time of combustion synthesis of the product. Moreover, the product is free from coordinated water molecules ( $\text{SnO}_2 \cdot n\text{H}_2\text{O}$ ) and its hydroxide linkage  $[\text{Sn}_4(\text{OH})_2 \cdot n\text{H}_2\text{O}]$  [30]. Present TGA results predicts only 13.4% of weight loss, which is in contradiction to both the reported theories that confirms the absence of both  $\text{Sn}_4(\text{OH})_2 \cdot n\text{H}_2\text{O}$  and  $\text{SnO}_2 \cdot n\text{H}_2\text{O}$  in the processed  $\text{SnO}_2$  compound [31].

The observed weight loss of about 13.4% is therefore assigned to the stray moisture atoms chemisorbed on the surface of the powder sample. Thermal study thus confirms the purity of the as-prepared material which also corroborates the results of x-ray diffraction measurements.

#### 4.3 XPS Analysis

Figure 3a shows the XPS wide scan spectra of the as-prepared  $\text{SnO}_2$  powder. It shows the presence of Sn 3d and O 1s peaks confirming the formation of  $\text{SnO}_2$  film with  $\text{Sn}^{4+}$  and  $\text{O}^{2-}$  states. Figures 3b and 3c show the narrow scan spectra of Sn 3d and O 1s present in  $\text{SnO}_2$ , which helps in fixing their binding energy and elemental state uniquely. From Figure 3b the binding energy of  $\text{Sn } 3d_{5/2}$  is observed at 489.05 eV which confirms the presence of  $\text{Sn}^{4+}$  bonding state the  $\text{SnO}_2$  lattice. The O 1s peak is located at 529.14 eV (Figure 3c), which is assigned to the  $\text{O}^{2-}$  bonding state of oxygen within the  $\text{SnO}_2$  lattice. The observation of only the above peaks, not additional peaks that can be attributed to other species such as  $\text{Sn}^{2+}$  or  $\text{O}^{-1}$ , confirms the formation of monophase  $\text{SnO}_2$  powder prepared in the present study.

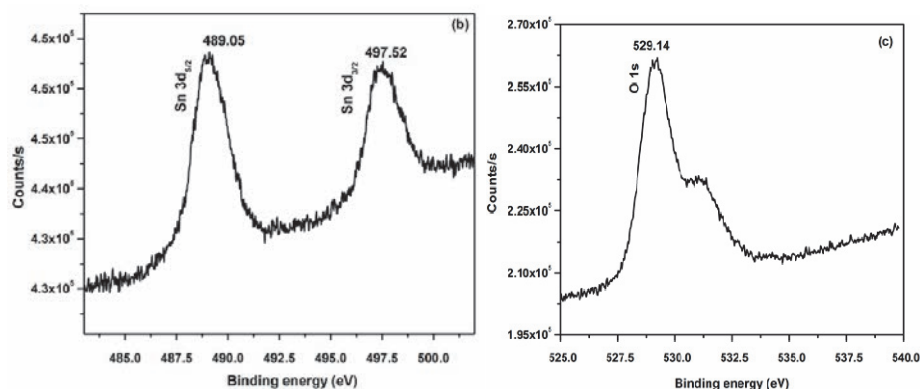


Fig. 3a, b and c: XPS analysis of wide scan and narrow scan mode of as-prepared  $\text{SnO}_2$

#### 4.4 SEM Analysis

Figures 4a and 4b show the typical SEM morphology of fully dense cassiterite  $\text{SnO}_2$  samples as-prepared and calcined at 300 °C, 500 °C and 800 °C respectively.

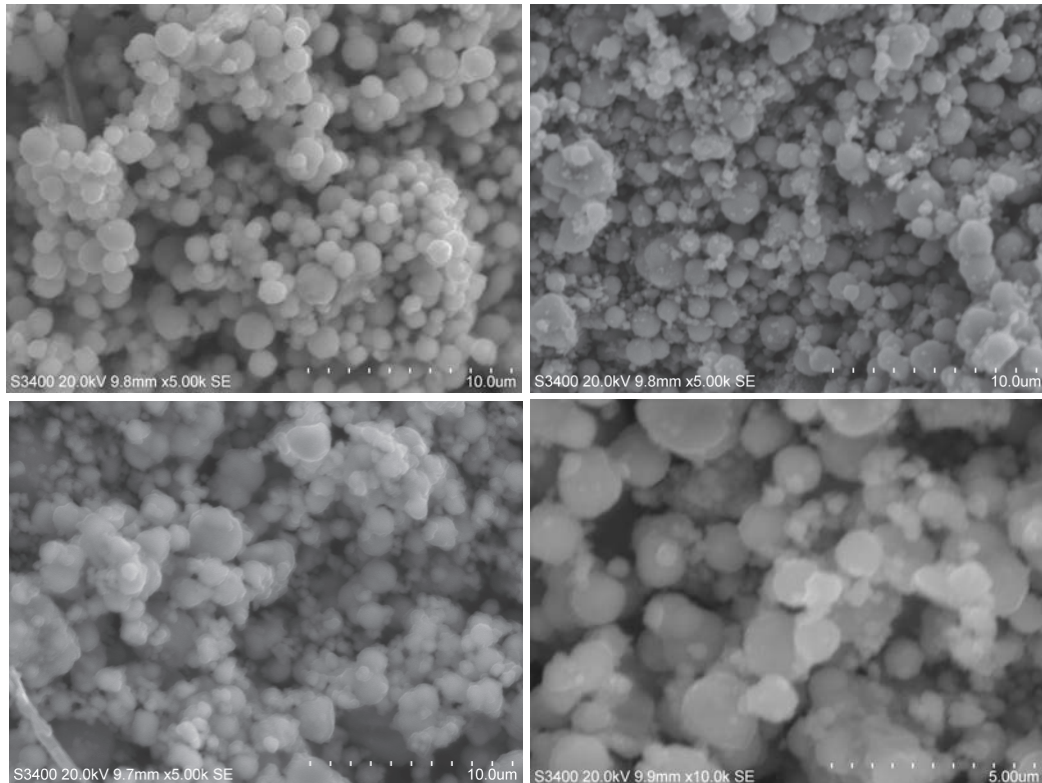
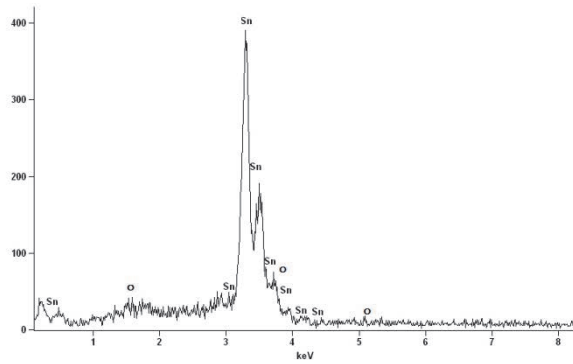


Fig. 4: SEM images of  $\text{SnO}_2$  (a) as prepared, (b)  $300\text{ }^\circ\text{C}$ , (c)  $500\text{ }^\circ\text{C}$  and (d)  $800\text{ }^\circ\text{C}$

Previous studies on nanocrystalline  $\text{SnO}_2$  have shown that pure metastable tetragonal phase can be stabilized when the crystallite size is below a critical size primarily due to very low surface energy associated with it. When the crystallite size exceeds this size, the transformation of metastable phase to monoclinic one occurs due to a decrease in surface energy. The grain size obtained in the as-prepared  $\text{SnO}_2$  powder seems to be above the critical size needed to stabilize the metastable tetragonal phase. In the present study, monoclinic phase could not be stabilized probably due to high degree of agglomeration and annealing among nanocrystals, which can reduce the surface energy. In addition, high enthalpy generated due to the high amount of urea also facilitates agglomeration and annealing among nanocrystals that favors the tetragonal phase as observed by other researchers [32].

#### 4.5 EDAX Analysis

The chemical composition of  $\text{SnO}_2$  nanopowders prepared at the optimized conditions was extracted from the energy dispersive X-ray spectrum (EDAX) which is shown in Figure 5. The EDS analysis exhibited clear peaks of only Sn and O elements, whereas no additional peaks were detected, which means that the as-prepared prepared powder is exempted from impurities that arise from the starting precursors like silicon and carbon.

Fig. 5: EDAX analysis of  $\text{SnO}_2$  powder

The atomic percentages of Sn and O elements present in the as-prepared powder are 77.99 and 22.01 mass.%, respectively, which indicates that the as-prepared  $\text{SnO}_2$  powder is very close to the stoichiometric compound:  $\text{Sn} = 76.03 + 1.96 = 77.99$  mass.% compared to the stoichiometry  $\text{Sn} = 118.71 / (118.71 + 2 * 15.9994) = 78.77$  mass.%, and the results are shown in Table 4.

Table 4: Atomic and mass percentages of elements in the as-prepared  $\text{SnO}_2$  as obtained by EDAX analysis

<i>Element Line</i>	<i>Net Counts</i>	<i>Atomic %</i>	<i>Mass Percent %</i>	<i>Formula</i>
<b>O K</b>	60	66.81	22.01	O
<b>Sn L</b>	11288	33.08	76.03	Sn
<b>Sn M</b>	310	0.11	1.96	Sn
<b>Total</b>		100.00	100.00	

#### 4.6 TEM Analysis

Numerous studies on nanocrystalline  $\text{SnO}_2$  have shown that pure metastable tetragonal and cubic phases can be stabilized at room temperature when the crystallite size is below a critical size primarily due to very high surface energy associated with it. When the crystallite size exceeds this size, the transformation of metastable phases to the monoclinic one occurs due to decrease in surface energy. Hence particle size analysis plays an important role in deciding the transformation of crystalline phases.

Figure 6a shows TEM micrograph of as-prepared  $\text{SnO}_2$  powder, which reflects the highly agglomerated powder having nearly spherical nanocrystals with facets of size around 17 nm. The crystallite size observed by TEM is in good agreement with that estimated by X-ray line broadening (10 nm for as-prepared to 30 nm after annealing at 800 °C). This study again favors for the evolution of tetragonal phase of the product using the proposed here the preparative conditions probably due to high degree of agglomeration which can reduce the surface energy. SAED pattern of this phase as shown in Figure 6b exhibits some rings made up of discrete spots, indicating the nanosized and highly polycrystalline nature of the as-prepared  $\text{SnO}_2$  particles. Multiple rings are seen in SAED spectrum, as expected from the XRD pattern. The bright-field image shown in Figure 6c, confirms that nanoparticles are spherical in shape and the narrow distribution of particle size. From Figure 6d, it was found that the majority of the nanoparticles have diameters between 15 and 22 nm,

which convincingly demonstrated the precise control over the diameter of the nanoparticles, which can be easily achieved by using monodispersed clusters, an important advantage of the combustion approach.

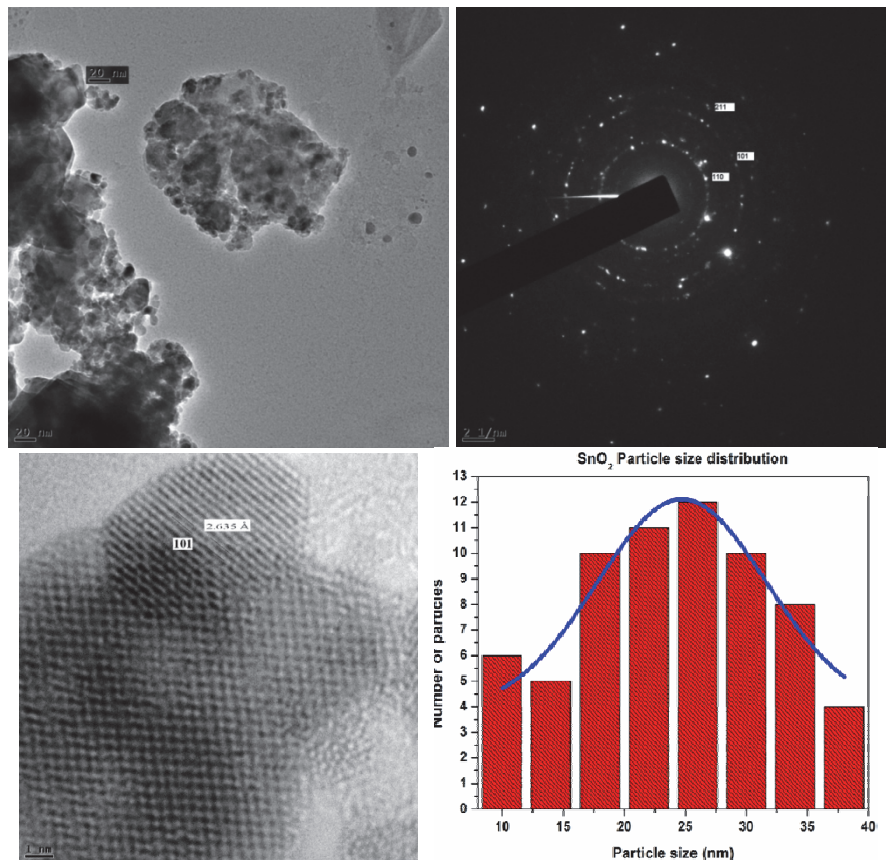
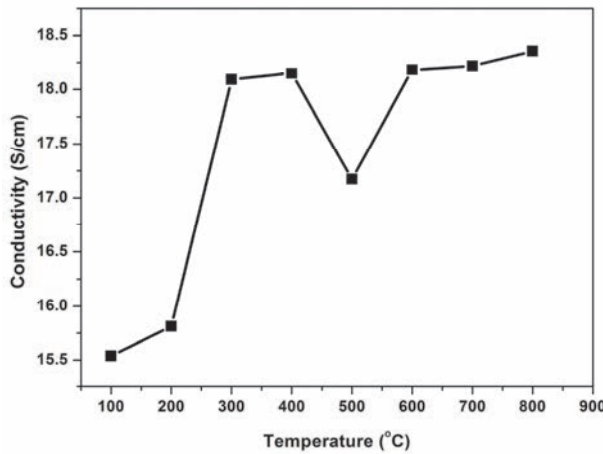


Fig. 6: (a) TEM analysis of as-prepared SnO<sub>2</sub> sample, (b) SAED pattern of SnO<sub>2</sub>, (c) Lattice planes of SnO<sub>2</sub> and (d) Particle size distribution of SnO<sub>2</sub>

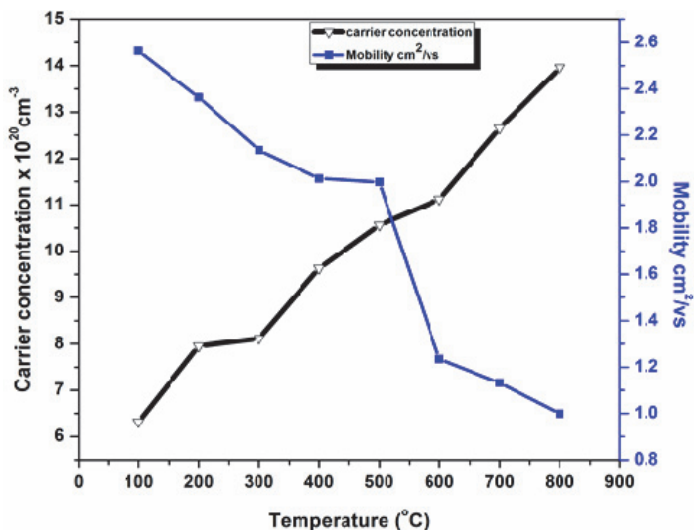
#### 4.7 Electrical Properties

The resistivity decreases significantly with annealing temperature up to 450°C, this behavior is good in agreement with the results reported in literature [33]. As a result, lower annealing temperature led to the formation of lower resistance. This is basically due to the increase of the mobility and/or carrier density at lower annealing temperature. The decrease in the resistivity with decreasing annealing temperature could be attributed to the improved crystalline nature of the particles. The decrease in annealing temperature may have led to more oxygen vacancies, resulting in an increase in carrier density due to the availability of pure tin to become ionized to donate electrons [34].

The carrier concentration and mobility of the as-prepared SnO<sub>2</sub> powders are shown in Figure 7. For the as-prepared particles, the carrier concentration decreases whereas mobility increases so that the lowest resistivity ( $4.936 \times 10^{-5} \Omega\text{cm}$ ) was obtained. The low carrier concentration for as-prepared powder was due to the oxygen vacancies being filled by the oxygen produced by electron-impact dissociation of water during combustion reaction. Extremely low mobility at 800°C can be attributed tentatively to scattering at grain boundaries and to grain volume because of oxygen deficiency.

Fig. 7: Conductivity of as-prepared  $\text{SnO}_2$  and annealed at 800°C

The as-prepared powder carrier concentration ( $13.96 \times 10^{20} \text{ cm}^{-3}$ ) decreases slightly ( $5.046 \times 10^{20} \text{ cm}^{-3}$ ) due to annealing up to 800°C. The carrier concentration during annealing gradually increases to reach a constant value around  $5-6 \times 10^{20} \text{ cm}^{-3}$ . Thus, the carrier concentration after thermal crystallization was dependent on the annealing temperature even after being subject to the crystallite size during the high-temperature and impurity phase formation. This result indicates that the porosity or the distribution of tin ions within crystals was under various annealing temperatures which changed the tetragonal phase. The annealing temperature led to a decrease in conductivity that can be attributed to insufficient crystal growth with a high defect concentration. As a result, the resistivity of the annealed powder was mainly determined by the carrier concentration which is shown in Figure 8.

Fig. 8: Mobility and carrier concentration of as-prepared  $\text{SnO}_2$  and annealed at 800°C

The lowest and highest resistivity is  $4.936 \times 10^5 \Omega\text{cm}$  and  $9.37 \times 10^4 \Omega\text{cm}$ , respectively shown in Table 5.

Table 5: Electrical properties of SnO<sub>2</sub> nanopowders

Annealing Temperature (°C)	Resistivity ( $\Omega \text{ cm}^{-1}$ )	Conductivity (s/cm)	Carrier Concentration $\times 10^{20} (\text{cm}^{-3})$	Mobility ( $\text{cm}^2/\text{VS}$ )
As-prepared	4.93E6	2.0284E-7	5.046	2.698
100	5.6E6	1.78571E-7	6.32	2.563
200	7.36E6	1.3587E-7	7.95	2.363
300	7.19E7	1.39082E-8	8.12	2.136
400	7.61E7	1.31406E-8	9.63	2.013
500	2.87E7	3.48432E-8	10.56	1.998
600	7.87E7	1.27065E-8	11.12	1.235
700	8.17E7	1.22399E-8	12.65	1.132
800	9.37E7	1.06724E-8	13.96	0.999

## 5. Conclusion

Pure and single phase nanocrystalline SnO<sub>2</sub> powder was successfully synthesized via a simple sol-gel combustion process using tin nitrate as precursor. The size of particles can be tuned from 15 to 20 nm by heating at different temperatures. The formation of SnO<sub>2</sub> nanograined powder with rutile tetragonal structure is observed for the as-prepared and also for 800°C heated powder. TEM results showed granular particles with a size of about 25 nm. HRTEM pictures have (110) and (101) planes and SAED pattern also shows these peaks confirming the formation of monophase SnO<sub>2</sub> powder with nano-crystallites. EDAX shows the presence of Sn and O and their presence in stoichiometric proportion.

## References

- [1] J. Rockenberger, U. Felde *et al.*, *J. Chem. Phys.* **112** (2000) 4296
- [2] L. Chou, Y. Cai *et al.*, *Appl. Catal. A: Gen.* **238** (2003) 185
- [3] P. T. Wierzchowski, L.W. Zatorski, *Appl. Catal. B: Environ.* **1352** (2003) 1
- [4] A. J. Moulson, J.M. Herbert, *Electroceramics*, Chapman & Hall, (1990)
- [5] Y. Shimizu, M. Egashira, *MRS Bull.* **24** (1999) 18
- [6] M. Kojima, F. Takahashi *et al.*, *Thin Solid Films* **392** (2001) 349
- [7] C. M. Lampert, *Sol. Ener. Mater.* **6** (1981) 1
- [8] J. F. Wang, Y.J. Wang *et al.*, *Mater. Sci. Eng. B* **96** (2002) 8
- [9] M.R.C. Santos, P.R. Bueno *et al.*, *J. Eur. Ceram. Soc.* **21** (2001) 161
- [10] T. E. Moustafid, H. Cachet, B. Tribollet, D. Festy, *Electrochim. Acta* **47** (2002) 1209
- [11] M. Okuya, S. Kaneko *et al.*, *J. Eur. Ceram. Soc.* **21** (2001) 2099
- [12] T.W. Kim, D.U. Lee *et al.*, *Phys. Chem. Solids* **63** (2002) 881
- [13] K.C. Song, Y. Kang, *Mater. Lett.* **42** (2000) 283
- [14] N. Nitta, S. Otani, M. Haradome, *J. Electron. Mater.* **9** (1980) 727
- [15] F. Li, L. Chen *et al.*, *Mater. Chem. Phys.* **73** (2002) 335
- [16] K. C. Song, J.H. Kim, *J. Colloid Interf. Sci.* **212** (1999) 193
- [17] G. Zhang, M. Liu, *J. Mater. Sci.* **34** (1999) 3213
- [18] J. H. Lee, S.J. Park, *J. Am. Ceram. Soc.* **76** (1993) 777
- [19] M. Bhagwat, P. Shah, V. Ramaswamy, *Mater. Lett.* **57** (2003) 1604
- [20] S. Baik, G. Sakai *et al.*, *J. Am. Ceram.Soc.* **83** (2000) 2983
- [21] F. Cabrera, D. Ardisson *et al.*, *Catalysis Today* **133** (2008) 800

- [22] J. M. Herrmann, F. Villain *et al.*, Applied Catalysis A: General **240** (2003) 177
- [23] V. Baranauskas, M. Fontan *et al.*, Sensors and Actuators **B 107** (2005) 474
- [24] M. S. Park, Y.-M. Kang *et al.*, Advanced Functional Materials, **18- 3** (2008) 455
- [25] Ayeshamariam, V. S. Vidhya *et al.*, Journal of Nanoelectronics and Optoelectronics , 06/2013, **8**:1-8
- [26] C. Huang, Z. Tang *et al.*, Cerm. Soc. **84** (2001) 1637
- [27] P.W. Cooper, S.R. Kurowski, Technology of Explosives, (1996)
- [28] Y. Taguchi, N. Saito, Colloids Surf. **A 153** (1999) 401
- [29] D. R. Lide, ed., CRC Hand book of Chemistry and Physics, CRC Press, 2005
- [30] A.Bonamartini, F.Bondioli, *et al.*, Chem. Mater. **13** (2001) 4550
- [31] C. C. Hwang, C.Y. Wu, *et al.*, Mater. Sci. Eng. **B 111** (2004) 49
- [32] O. Vasykiv, Y. Sakka, J. Am. Ceram. Soc. **84** (2001) 2489
- [33] R. D. Purohit, B.P. Sharma *et al.*, Mater. Res. Bull. **36** (2001) 2711
- [34] G. Granqvist, A. Hultaker, Thin Solid Films **411** (2002) 1

